Marquette University
e-Publications@Marquette

Biomedical Engineering Faculty Research and Publications

Biomedical Engineering, Department of

Non-common Path Aberration Correction in an Adaptive Optics Scanning Ophthalmoscope

Yusufu N. Sulai
University of Rochester

Alfredo Dubra
Marquette University

Non-Common Path Aberration Correction in an Adaptive Optics Scanning Ophthalmoscope

Yusufu N. Sulai

The Institute of Optics, University of Rochester
Rochester, NY

Alfredo Dubra

Department of Ophthalmology, Medical College of Wisconsin
Department of Biophysics, Medical College of Wisconsin
Department of Biomedical Engineering, Marquette University
Milwaukee, WI

Abstract

The correction of non-common path aberrations (NCPAs) between the imaging and wavefront sensing channel in a confocal scanning adaptive optics ophthalmoscope is demonstrated. NCPA correction is achieved by maximizing an image sharpness metric while the confocal detection aperture is temporarily removed, effectively minimizing the monochromatic aberrations in the illumination path of the imaging channel. Comparison of NCPA estimated using zonal and modal orthogonal wavefront corrector bases provided wavefronts that differ by $\sim\lambda/20$ in root-mean-squared ($\sim\lambda/30$ standard deviation). Sequential insertion of a cylindrical lens in the illumination and light collection paths of the imaging channel was used to compare image resolution after changing the wavefront correction to maximize image sharpness and intensity metrics. Finally, the NCPA correction

was incorporated into the closed-loop adaptive optics control by biasing the wavefront sensor signals without reducing its bandwidth.

OCIS codes: (110.1080) Active or adaptive optics, (170.4460) Ophthalmic optics and devices

1. Introduction

Adaptive optics (AO) allows for the measurement and control of monochromatic aberrations in optical instruments. Although first proposed for compensating the wavefront distortions induced by atmospheric turbulence in astronomical telescopes [1,2], AO has found multiple applications including: high-power lasers [3], ophthalmic imaging [4], vision research [5] and microscopy [6]. The control of the monochromatic aberrations can be performed either in a sensorless fashion, using metrics that directly indicate the instrument's performance [6], or with wavefront sensors such as the shearing interferometer [7,8], the pyramid sensor [9,10] and the Shack-Hartmann sensor [11,12]. Sensorless AO has traditionally been used when aberrations are slow-varying relative to the AO closed-loop bandwidth; or wavefront sensors have limited success or add unacceptable complexity. To date, AO ophthalmoscopes have been mostly implemented using wavefront sensors [4,13–25], with few sensorless implementations [26–29].

In AO ophthalmoscopes with wavefront sensors, a portion of the optical path leading to the wavefront sensor is inevitably different from that leading to the imaging detector(s). This gives rise to non-common path aberrations (NCPAs) that could lead to non-negligible performance degradation if left uncorrected [28,30]. These NCPAs can be due to optical element theoretical performance, manufacturing imperfections or distortion due to mechanical mounting with excessive pressure. In mechanically and thermally stable AO ophthalmoscopes, NCPAs can be considered static unless the relative focus between the imaging and wavefront sensor channels is changed [30,31].

Although NCPAs in AO ophthalmoscopy are widely acknowledged [13,28,29,32–35], their correction in point-scanning instruments with a wavefront sensor have only been demonstrated once [28]. Hofer et al. corrected NCPAs by driving the wavefront corrector to maximize the

photon count through a confocal aperture, similar to other sensorless AO techniques [27,36,37]. This approach is only optimal both in terms of maximizing signal strength and image resolution in a small number of scenarios, including non-linear imaging techniques with confocal apertures much larger than the Airy disk or linear imaging techniques with perfectly overlapping illumination and imaging paths [28]. In linear confocal imaging techniques such as that used by Hofer el al., the difference between NCPAs between the illumination and imaging paths dictates that maximizing image intensity does not guarantee the best image resolution. This often unappreciated point is critical for image resolution maximization and it is the motivation for this work.

In what follows, we propose to correct NCPAs in scanning AO ophthalmoscopes through the maximization of an image sharpness metric while the confocal detection aperture is temporarily removed from the optical path. We first discuss how the proposed method follows naturally from the calculation of the point spread function (PSF) of a confocal point scanning instrument. This is followed by a brief description of the AO scanning light ophthalmoscope (AOSLO) and the experimental methods used for this work. Then, a known NCPA is induced by inserting a cylindrical lens in either the illumination or the light collection path of the imaging channel, measured and then corrected to illustrate how the sharpness-maximization-driven approach compares to an intensity-maximization-driven approach. Finally, the AOSLO native NCPAs are measured and used to bias the Shack-Hartmann wavefront sensor (SHWS) to achieve simultaneous aberration correction of the illumination path of the imaging channel and a living eye when closing the AO control loop.

2. Theory

2.1 Resolution in confocal point scanning ophthalmoscopes

The incoherent intensity PSF of the imaging channel in a confocal point scanning instrument is given by

$$h \propto h_{\text{illumination}}(h_{\text{collection}} \otimes p),$$

(1)

where $h_{illumination}$ is the intensity PSF of the illumination path, $h_{collection}$ is that of the light collection path, p is the confocal aperture transmission function (or the effective detector size at the image plane) and ⊗ denotes convolution [38]. The convolution blurs the PSF of the imaging path, increasing its full-width at half-maximum (FWHM) by more than 20, 120 and 450% for confocal detection apertures greater than 0.5, 1.0 and 2.0 Airy disks in diameter, respectively. Since in most instruments the confocal aperture (pinhole) diameter is comparable to or larger than the Airy disk, the PSF of the instrument and thus the image sharpness, are mostly determined by the size of the illumination PSF and not the imaging PSF. Therefore, when $h_{illumination} \neq h_{collection}$, maximizing image intensity does not necessarily lead to optimum image resolution. Equation (1) also indicates that removing the confocal aperture (making the instrument equivalent to a bright field instrument replacing the illumination PSF with the collection PSF), the effect of $h_{collection}$ on the instrument PSF is effectively cancelled (blurred). This means that one could temporarily remove the confocal aperture to estimate the NCPAs between the light collection path of the wavefront sensing channel (which is what the wavefront sensor measures) and the light collection path of the imaging channels. Following NCPA estimation, the confocal pinhole can be placed back for image acquisition. We therefore propose NCPA estimation by temporarily removing the confocal aperture, while driving the wavefront corrector to maximize an image sharpness metric using a test object. It is important to note that the use of a sharpness rather than intensity metric is critical, as the latter would not be substantially affected by the wavefront corrector given the large effective size of the confocal aperture. The difference between the wavefront corrector signals that minimize the wavefront sensor error signals and those that maximize the image sharpness metric provides the NCPAs correction. Thus, replacing the confocal aperture and biasing the wavefront sensor signals to account for the NCPAs provides AO correction that minimizes aberrations in the illumination path of the imaging channel, and thus maximizing image resolution.

2.2 Image sharpness metric

The most common approach for estimating and correcting NCPAs in AO imaging instruments is to systematically change the

signals controlling the wavefront corrector(s) so as to maximize an image quality metric when imaging a stationary object [6,28,39,40]. This maximization is mostly determined by: the image metric [28,37,41–46], the wavefront corrector mode basis [47], the algorithm used to search for the metric maximum in the wavefront corrector space [48] and the test object [43].The image sharpness metric used in this work is the normalized discrete version of the quadratic intensity sum described by Muller and Buffington,

$$M = \sum_i I_i^2 \Big/ \left(\sum_i I_i \right)^2,$$

(2)

where I_i denotes the intensity of the i-th pixel and the summation is performed over the entire image [41]. The normalization accounts for intensity variations that might arise due to vignetting, intensity and sensitivity fluctuations in the light source and detector, respectively.

2.3 Deformable mirror mode bases

The wavefront corrector in the AOSLO was a 97 actuator continuous membrane deformable mirror (DM; ALPAO, Montbonnot, France), controlled using one of two bases that are orthogonal in the DM actuator space. The first basis was formed by each actuator's influence function, while the second basis consisted of the modes from the singular value decomposition of the experimentally determined AO response matrix. In what follows, we refer to these bases as zonal and modal, respectively. The elements of the modal basis are shown in Fig. 1 as wavefront maps in decreasing singular value order, assuming a 2-dimensional Gaussian influence function with 50% of the peak amplitude at the nearest actuator. It is worthwhile noting that the 97th mode, which is similar to piston, is removed from all the wavefront maps presented later, as it does not affect image quality.
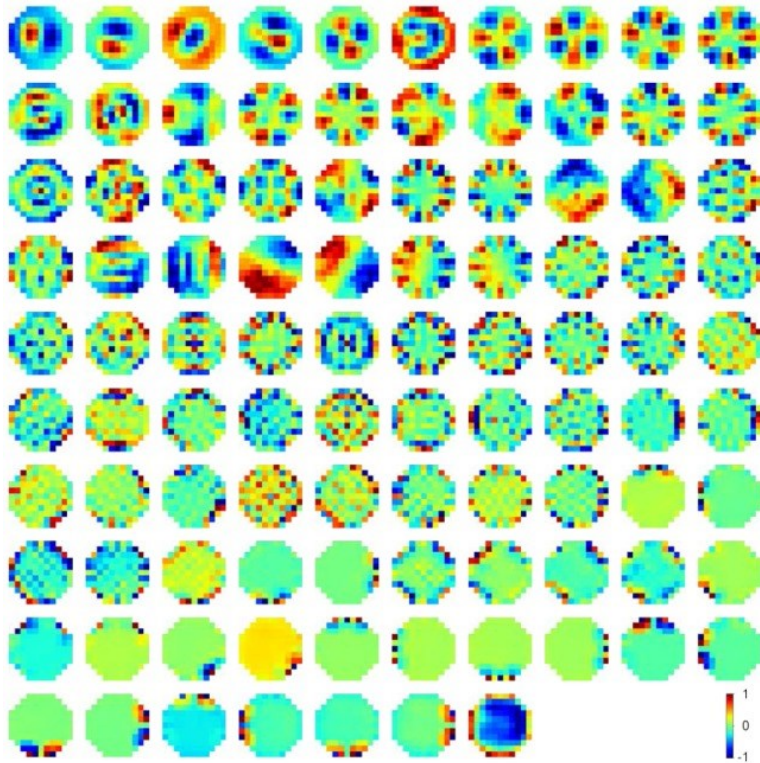
Fig. 1 Normalized deformable mirror modes derived from the response matrix defined by the Shack-Hartmann wavefront sensor used in this work [20], ordered from left to right and top to bottom according to decreasing singular value. Each pixel in the diagrams above represents the amplitude of a single deformable mirror actuator.

3. Methods

3.1 Adaptive optics scanning light ophthalmoscope

The confocal point scanning instrument used in this work was a previously described AOSLO [20] (Fig. 2), equipped with two coaxial light sources for wavefront sensing (850 nm) and imaging (790 nm). Light is coupled into the optical path common to the imaging and wavefront sensing channels using a 90/10 (transmission/reflection) beam splitter wedged at 0.5° in order to vignette the undesired reflection from the second surface. The illuminating beams are raster scanned on the retina by using two optical scanners with orthogonal rotation axes. Light backscattered by the retina retraces its path and is de-scanned on its way to the light detectors. The wavefront sensing and imaging wavelengths are separated by a dichroic mirror before reaching the SHWS and the imaging light detector (photomultiplier).

The NCPAs between the illumination, light collection and wavefront sensing paths arise from the optical elements in the areas highlighted in the AOSLO schematic shown in Fig. 2.
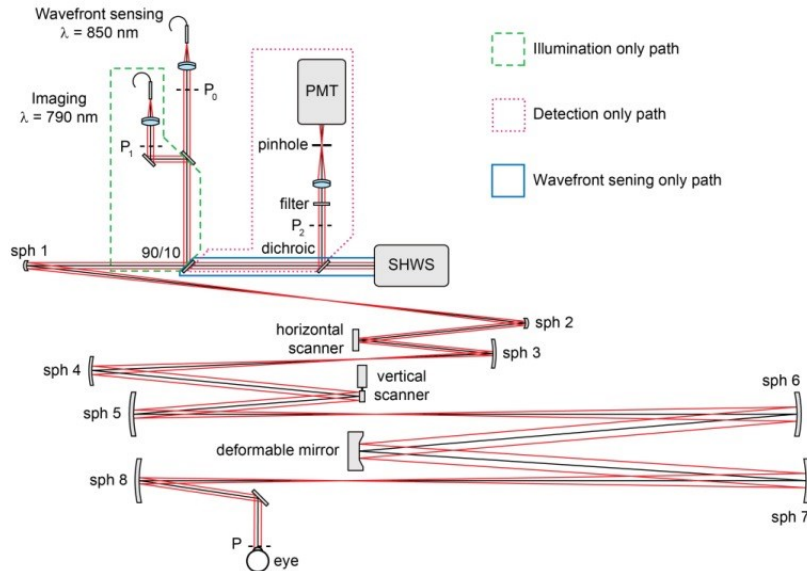
Fig. 2 AOSLO schematic where PMT stands for photomultiplier, SHWS for Shack-Hartmann wavefront sensor, and sph for spherical mirror. The letter P indicates a pupil conjugate plane, in addition to those corresponding to the deformable mirror, the optical scanners and the SHWS. The optical elements contributing to the non-common path aberrations between the SHWS and either the illumination or the collection paths of the imaging channel are highlighted with boxes as indicated by the key. The pupil planes P_1 and P_2 in the imaging channel were used in the validation experiment to place a cylindrical lens (see section 4).

3.2 Sharpness metric sensitivity

Prior to the estimation of the NCPA, the sensitivity of the sharpness metric to the zonal and modal basis elements was determined using a piece of paper in the back focal plane of an achromatic doublet (19 mm focal length) as a test object, after removing the confocal pinhole. The paper was placed perpendicular to the AOSLO optical axis to avoid having features in multiple focal planes, which would potentially affect the convergence of the sharpness maximization algorithm. The sharpness metric curves for the AOSLO were generated using the images of the paper over the entire amplitude range of each mode, resulting in the plots shown in Figs. 3 and and4Fig.4. The mode ranges were centered on the DM

voltages that minimize the aberrations in the SHWS channel. The inverse of the width of each curve's peak can be interpreted as the sensitivity of the metric to that particular mode. For the zonal basis (Fig. 3), the metric changes across the full actuator range were only ~1%, and mostly determined by the actuator distance to the center of the DM, with the actuators at the center affecting the metric the most. Similarly, the plots for the modal basis show only up to a 2% change in the metric over the full mode range (Fig. 4). Due to the fact that the modes are in decreasing order of singular value, there is a clear decrease in sensitivity with increasing mode number, as expected.
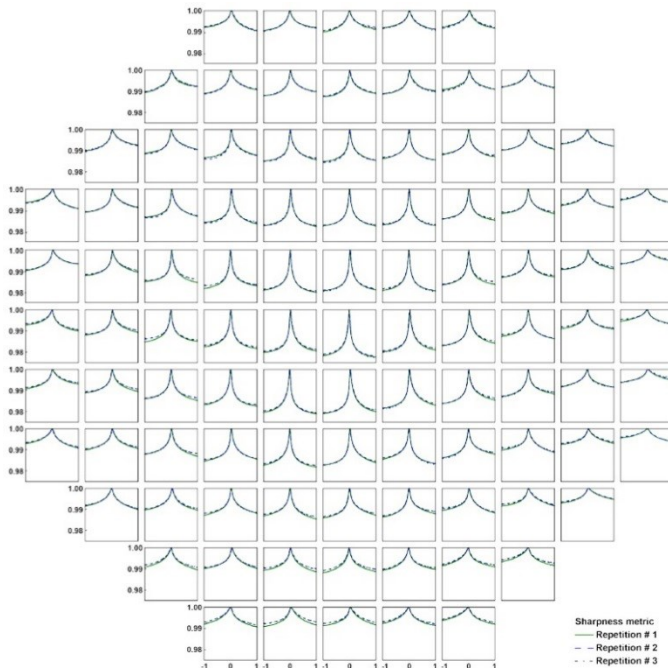

Fig. 3 Sharpness metric normalized to peak value *vs.* normalized actuator stroke for the 97 actuators of the Alpao DM used in this study. The plots are spatially arranged to reflect actuator placement on the DM surface. The repeatability of these curves was better than 1% over 3 repetitions.
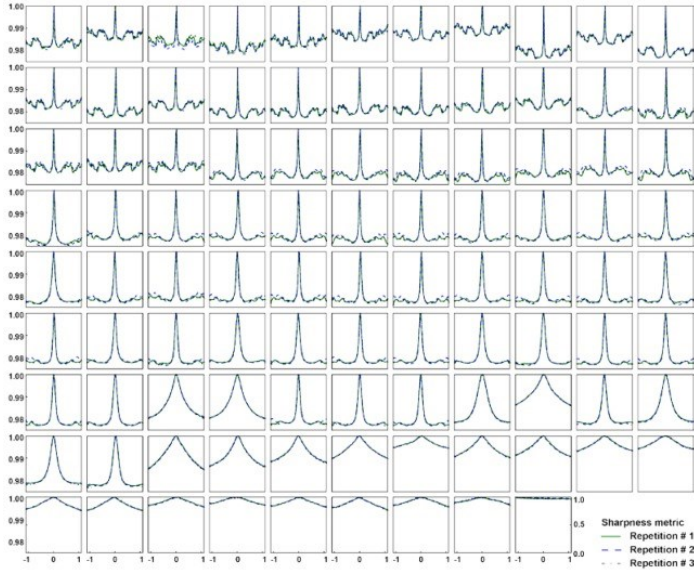
Fig. 4 Sharpness metric normalized to peak value *vs.* normalized stroke for the 97 modes of the Alpao DM used in this study. The plot arrangement corresponds to the modes shown in decreasing singular value (as shown in Fig. 1). The repeatability of these curves was better than 1% over 3 repetitions.

3.3 NCPA correction algorithm

The natural choice of wavefront corrector amplitudes for initiating the NCPA estimation is those that minimize the wavefront sensor signals. These can be determined by closing the AO correction loop using the model eye mentioned above. If the imaging and wavefront sensing channels were intentionally out of focus relative to each other, one could improve on the initial condition by adding the focus offset that would bring the object, in this case paper, into subjective focus.

The sequence of steps followed to estimate the NCPAs by maximizing the sharpness metric for each DM mode is detailed in Fig. 5. This is accomplished by sequentially incrementing the amplitude of each mode over a range given by the width of the peak in the corresponding sensitivity curves (Figs. 3 and and4).4). After applying each new set of DM control signals, a 20 ms delay allowed for the DM surface to settle, before an image of the paper was acquired and the sharpness metric calculated. This process was repeated for all the amplitudes in the selected range and the value that provided highest sharpness metric value was recorded. If the mode amplitude

corresponding to the sharpest image was close to the edge of the selected range, the range was re-centered on this value and the process repeated. The cycling through all of the DM modes was repeated four times, each time using the output of the last iteration as the starting point for the next one and also shrinking the range of amplitudes searched by 50%.
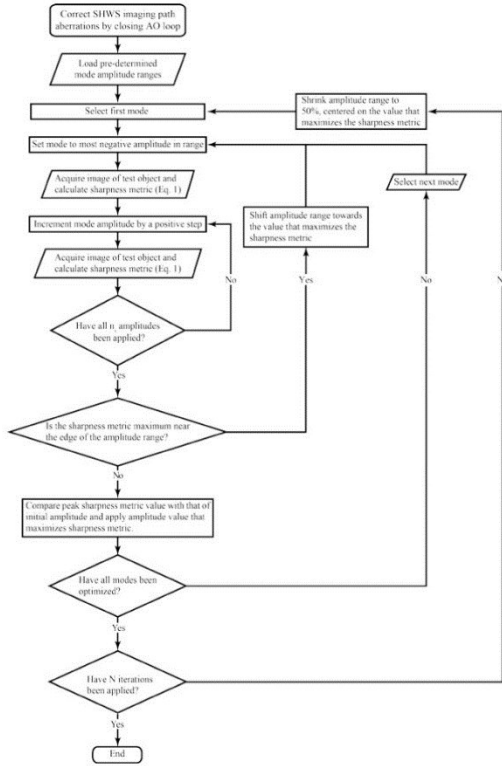

Fig. 5 AOSLO non-common path aberration estimation algorithm for finding the optimal amplitudes for a given DM set of modes. The rounded rectangles are starting/ending points, parallelograms are inputs/outputs, edged rectangles are operations and diamonds are questions.

After determining the wavefront corrector signal vector that maximizes the image sharpness ($\mathbf{x}_{\text{Illumination}}$), the NCPAs in DM space ($\mathbf{x}_{\text{NCPA}}$) was calculated as

$$\mathbf{x}_{\text{NCPA}} = \mathbf{x}_{\text{Illumination}} - \mathbf{x}_{\text{SHWS}},$$

(3)

with $\mathbf{x}_{\text{SHWS}}$ being the DM signals which correct the aberrations of the entire wavefront sensor path. Finally, in order to account for the

NCPAs when closing the AO loop, the SHWS signals are biased by the spot displacements that would result from multiplying $\mathbf{x}_{NCPA}$ by the AO response matrix [27] and removing piston, tip and tilt.

3.4 Experiments

In order to demonstrate the proposed method, we performed three experiments. First, we compared the use of an image sharpness metric after removal of the confocal aperture against the maximization of image intensity through a one Airy disk diameter confocal pinhole [27,28]. This was accomplished by intentionally exaggerating the NCPA through the placement of a 0.25 diopter (D) cylindrical lens in a pupil plane in a portion of the imaging channel that does not overlap with that of the SHWS imaging path (either in P_1 or P_2 in Fig. 2). In the second experiment, we tested the convergence, stability and repeatability of the proposed method using the zonal and modal bases to correct the AOSLO native NCPAs, followed by the insertion of a known NCPA through the use of the previously used cylindrical lens. Finally, a human subject was imaged using the traditional SHWS correction and the NCPA-biased correction after measuring and correcting the system NCPAs (i.e. without using any cylindrical lenses) and using a 1.0 Airy disk confocal aperture.

A 39-year-old male subject with mild refractive error (−0.75 D sphere, 2.0 D cylinder) was recruited for the study, which was approved by the Institutional Review Board at the Medical College of Wisconsin. The nature and possible risks of the study were explained after which written consent was obtained. The pupil of the left eye was dilated and cycloplegia was induced with topical application of one drop of phenylephrine hydrochloride (2.5%) and one drop of tropicamide (1%). The subject's head was stabilized with a bite bar attached to a three-axis translation stage used to align the AOSLO exit pupil with the entrance pupil of the subject's eye. Photoreceptor image sequences of 150 frames were acquired at 0.5° temporal and superior to fixation while closing the AO-loop. For each sequence, the 50 frames with highest normalized cross-correlation when compared against a manually selected reference frame were registered [49] and averaged to increase signal to noise ratio.

4. Results

4.1 Image intensity maximization in confocal imaging

The images and plots in Fig. 6 show how introducing a 0.25 D cylindrical wavefront as NCPA in the illumination path of the AOSLO imaging channel, results in a more substantial image blur than when placed in the imaging path, whether using the SHWS correction or an intensity driven NCPA correction. This is in agreement with our observation about the PSF calculation, in that it is the monochromatic aberrations in the illumination path that have the most impact in the image sharpness. This simple experiment also illustrates how the maximization of the intensity at the confocal pinhole, as implemented by Hofer et al [28], does not necessarily provide the highest image resolution.
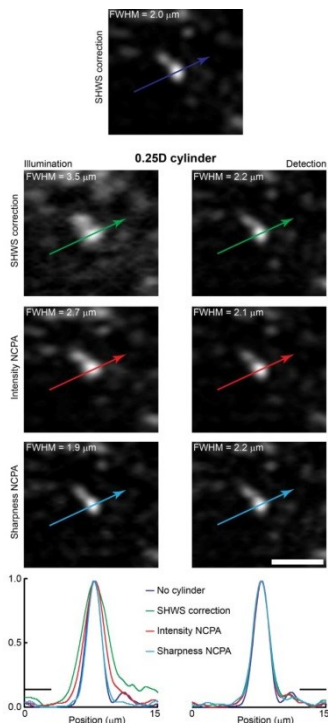

Fig. 6 Central portions of AOSLO images showing small features on the surface of a piece of paper, acquired using a one Airy disk diameter confocal pinhole. The top image was collected with the SHWS-driven correction. The images below show the same feature with SHWS-, intensity metric- and sharpness metric-driven correction, respectively, when placing a cylindrical lens (to induce a known NCPA) in the illumination and collection paths of the AOSLO imaging channel (see pupil planes P₁

and P_2 in Fig. 2). The bottom plots show intensity profiles indicated by the lines across the images above, normalized to their peak intensity. Scale bar is 10 μm or 2.1 Airy disk diameters.

4.2 Image sharpness maximization in bright-field imaging

Figure 7 shows the image sharpness metric described above (without the confocal aperture in front of the light detector) as each zonal or modal basis element is optimized to maximize the metric, and thus correct for the AOSLO native NCPA. Each estimation process consists of four successive iterations over the entire wavefront corrector basis shrinking the search range by 50% each iteration. This process was repeated three times, in order to gain some understanding of the convergence, stability and repeatability of the method. Ignoring the rapid oscillations due to measurement noise (e.g., discrete mode range sampling and image digitization), the curves slow trend suggest that the modal correction (blue curves in Fig. 7) is more repeatable and stable than the zonal correction (red curves), although the zonal approach seems to converge faster to the final metric value region. We recognize that the poor repeatability in the metric value is mostly due to a reduction in PMT signal resulting from continuous exposure to light, potentially combined with a small offset in the image digitization electronics (frame grabber). These factors change the image sharpness metric values by a small percentage (< 0.15%), which is comparable to the metric measured changes observed in the NCPA estimation (~0.1-0.2%). Irrespective of the actual metric value, the estimated NCPA, however, seems to be immune to this slow PMT sensitivity change, as the repeatability of the wavefront maps in Figs. 8 and 9 illustrate. The maps also suggest that NCPA correction is achieved after a single iteration through either wavefront corrector basis, with subsequent iterations providing little if any clear improvement, given the small NCPA in the tested AOSLO.
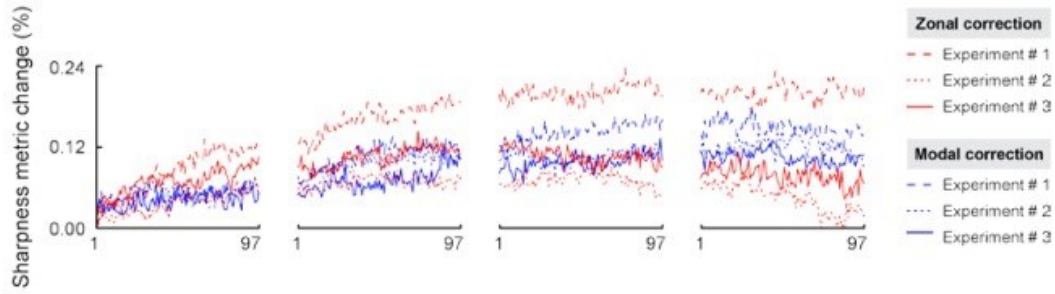
Fig. 7 Cumulative image sharpness metric change during the NCPA estimation (each curve of the same color corresponds to one of 3 repetitions). The metric change is relative to the wavefront that minimizes the SHWS aberrations path.
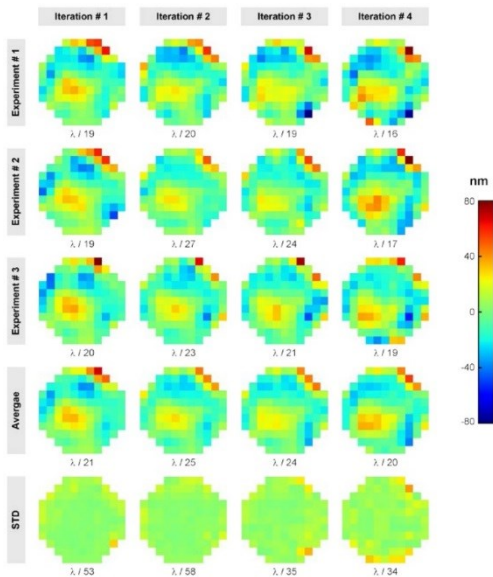

Fig. 8 NCPA AOSLO wavefront maps and RMS estimated using a wavefront corrector zonal basis. The top three rows show three repetitions of the iterative NCPA estimation, while the fourth and fifth rows show their corresponding averages and standard deviation.

The root-mean-square (RMS) of the wavefront maps in Figs. 8 and and9Fig.9 indicate that the NCPAs wavefront RMS in our AOSLO are approximately $\lambda/20$, which is below the diffraction limit according to Marechal's criterion ($\lambda/14$), in agreement with the fact that no noticeable differences can be seen between the representative images of the paper shown in Fig. 10. The wavefront maps and RMS values in the fourth and fifth rows of Figs. 8 and and99 indicate that the NCPA estimation is repeatable to within approximately $\lambda/30$, with the largest variation coming from the actuators at the DM edge.
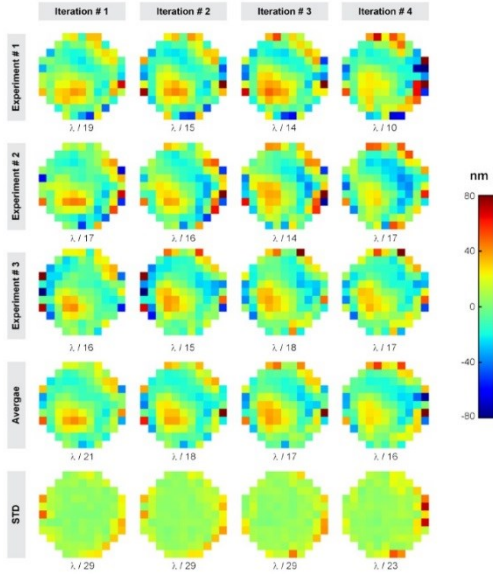
Fig. 9 NCPA AOSLO wavefront maps and RMS estimated using a wavefront corrector modal basis. The top three rows show three repetitions of the iterative NCPA estimation, while the fourth and fifth rows show their corresponding averages and standard deviation.
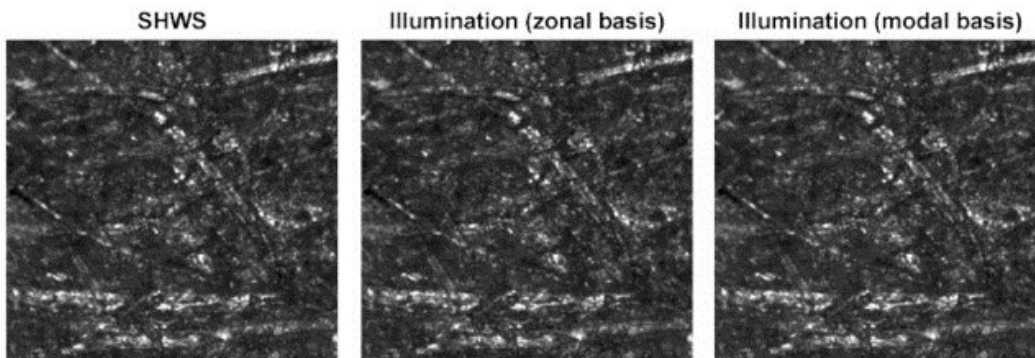

Fig. 10 AOSLO images of paper (~330 μm across) after correcting the aberrations on the SHWS optical path and the illumination path using the image sharpness metric describe above and the zonal and modal DM basis.

Finally, when placing a 0.25 D cylindrical lens in a pupil plane only affecting the illumination path (P$_1$ in Fig. 2) both the correction using the zonal and modal bases resulted in similar wavefront maps despite converging to different image sharpness metric values (Figs. 11 and and12Fig.12). The larger differences between the wavefronts correspond to the DM outer actuators, as in the previous experiment. This can be explained by the fact that these actuators are only partially within the pupil and thus have less of an impact in the image metric

(see Fig. 3). The estimated wavefront RMS is comparable to the λ/1.67 theoretical prediction for a centered 0.25 D cylindrical lens (our lens was slightly decentered due to mechanical constraints).
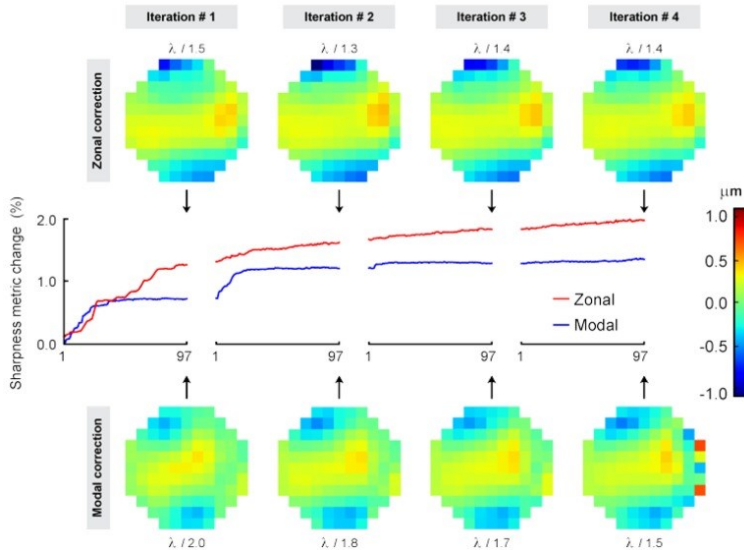

Fig. 11 Cumulative image sharpness metric plots when correcting for a 0.25 D cylindrical lens over four iterations through the entire set of modes/actuators. The predicted RMS wavefront error is shown above (zonal) or below (modal) the wavefront maps at the end of each iteration.
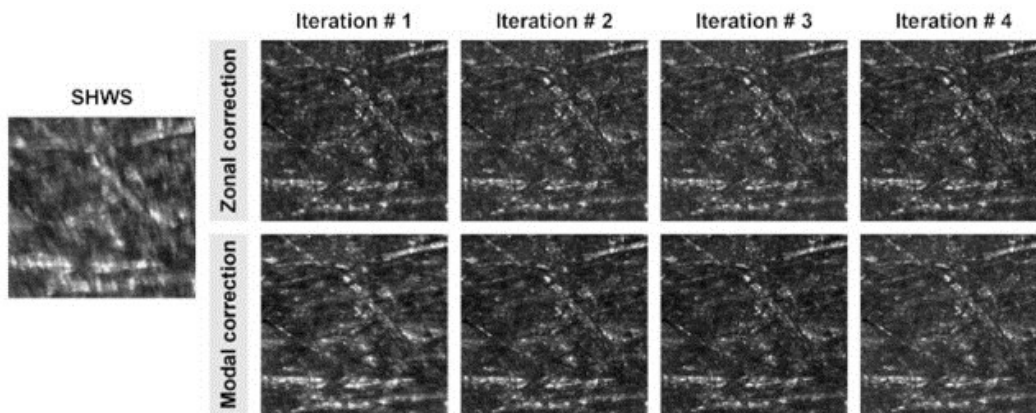

Fig. 12 AOSLO images of paper with a 0.25D cylindrical lens acquired before (SHWS path correction only) and after four NCPA correction iterations (with correction of the illumination path of the imaging channel).

4.3 Human retinal imaging

In agreement with the findings from the previous section, the photoreceptor images acquired with and without correction of the native AOSLO NCPAs (Fig. 13) show similar levels of detail, other than for individual cone photoreceptor intensity variations. This intensity fluctuation is a well-known phenomenon that can be observed in both cone and rod photoreceptors [50,51]. Comparison of the power spectra radial averages [52,53] and autocorrelation function width [53] (data not shown) in images collected with and without NCPA correction yielded undistinguishable differences, as expected, given the small measured NCPAs (RMS $\sim\lambda/16$).
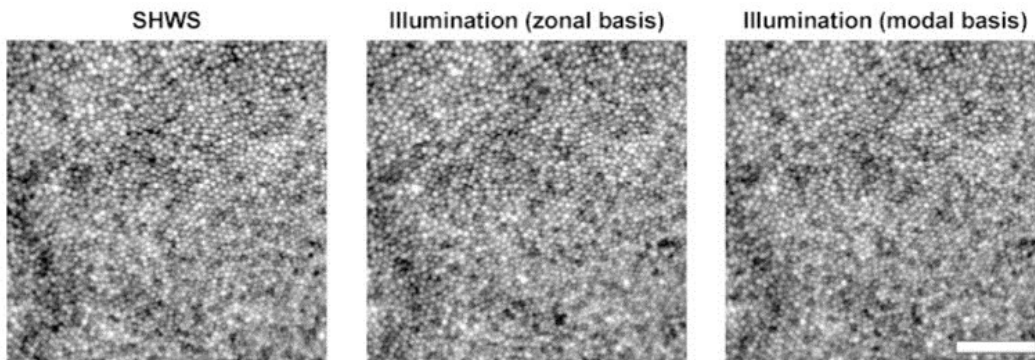
Fig. 13 AOSLO images showing the photoreceptor mosaic in a logarithmic intensity scale at 0.5° temporal and superior to fixation in subject JC_0486. These images were collected with aberration correction over the SHWS and the illumination paths (using zonal and modal wavefront corrector basis). Scale bar is 50 µm.

5. Conclusions

A method for estimating and correcting NCPAs between the wavefront sensing and the illumination paths of an imaging channel in a confocal point scanning imaging instrument was demonstrated. In this approach, an image sharpness metric was maximized by iterating through the modes of one of two different wavefront corrector bases. The use of a sharpness metric and the temporary removal of the confocal aperture are critical to achieving NCPA correction that maximizes image resolution, as opposed to image intensity. The NCPA estimation in this particular instrument was repeatable with an RMS smaller than Maréchal's classical diffraction limit. It is worth noting that in AO ophthalmoscopes with multiple imaging channels, one might

bias the wavefront sensor using different NCPA measurements depending on the imaging channel that is deemed more critical at the time. Moreover, different NCPA calibrations should be considered when changing the focus of the illumination relative to the wavefront sensor, given that monochromatic aberrations vary with degree of collimation (vergence).

In summary, NCPA estimation and/or correction in point scanning AO imaging instruments is simple, straightforward and does not require hardware modifications, other than for temporarily removing the confocal aperture during the NCPA estimation. It would therefore seem reasonable to evaluate the NCPA for each imaging channel of the AO ophthalmoscope. If the NCPA wavefront RMS was found to be larger than $\lambda/14$, then it would be recommended to incorporate the NCPAs as a fixed bias to the wavefront sensor.

Acknowledgments

References and links

1. Babcock H. W., "The possibility of compensating astronomical seeing," Publ. Astron. Soc. Pac. 65, 229–236 (1953).10.1086/126606
2. Hardy J. W., Adaptive Optics for Astronomical Telescopes, Oxford Series in Optical and Imaging Sciences (Oxford University Press, New York, 1998).
3. Chanteloup J. C., Baldis H., Migus A., Mourou G., Loiseaux B., Huignard J. P., "Nearly diffraction-limited laser focal spot obtained by use of an optically addressed light valve in an adaptive-optics loop," Opt. Lett. 23(6), 475–477 (1998).10.1364/OL.23.000475

4. Liang J., Williams D. R., Miller D. T., "Supernormal vision and high-resolution retinal imaging through adaptive optics," J. Opt. Soc. Am. A 14(11), 2884–2892 (1997).10.1364/JOSAA.14.002884

5. Williams D., Yoon G. Y., Porter J., Guirao A., Hofer H., Cox I., "Visual benefit of correcting higher order aberrations of the eye," J. Refract. Surg. 16(5), S554–S559 (2000).

6. Neil M. A. A., Juškaitis R., Booth M. J., Wilson T., Tanaka T., Kawata S., "Adaptive aberration correction in a two-photon microscope," J. Microsc. 200(2), 105–108 (2000).10.1046/j.1365-2818.2000.00770.x

7. Wyant J. C., "Use of an ac heterodyne lateral shear interferometer with real-time wavefront correction systems," Appl. Opt. 14(11), 2622–2626 (1975).10.1364/AO.14.002622

8. Hardy J. W., Lefebvre J. E., Koliopoulos C. L., "Real-time atmospheric compensation," J. Opt. Soc. Am. 67(3), 360–369 (1977).10.1364/JOSA.67.000360

9. Ghedina A., Cecconi M., Ragazzoni R., Farinato J., Baruffolo A., Crimi G., Diolaiti E., Esposito S., Fini L., Ghigo M., Marchetti E., Niero T., Puglisi A., "On-sky test of the pyramid wavefront sensor," in Proc. SPIE 4839, Adaptive optical system technologies II (2003), 869–877.

10. Chamot S. R., Dainty C., Esposito S., "Adaptive optics for ophthalmic applications using a pyramid wavefront sensor," Opt. Express 14(2), 518–526 (2006).10.1364/OPEX.14.000518

11. Shack R. V., Platt B. C., "Production and use of a lenticular Hartmann screen," J. Opt. Soc. Am. 61, 656 (1971).

12. Liang J., Grimm B., Goelz S., Bille J., "Objective measurement of the wave aberrations of the human eye using a Hartmann-Shack wavefront sensor," J. Opt. Soc. Am. A 11, 1949–1957 (1994).10.1364/JOSAA.11.001949

13. Roorda A., Romero-Borja F., Donnelly Iii W., Queener H., Hebert T., Campbell M., "Adaptive optics scanning laser ophthalmoscopy," Opt. Express 10(9), 405–412 (2002).10.1364/OE.10.000405

14. Hermann B., Fernández E. J., Unterhuber A., Sattmann H., Fercher A. F., Drexler W., Prieto P. M., Artal P., "Adaptive-optics ultrahigh-resolution optical coherence tomography," Opt. Lett. 29(18), 2142–2144 (2004).10.1364/OL.29.002142

15. Zhang Y., Rha J. T., Jonnal R. S., Miller D. T., "Adaptive optics parallel spectral domain optical coherence tomography for imaging the living retina," Opt. Express 13(12), 4792–4811 (2005).10.1364/OPEX.13.004792

16. Zawadzki R. J., Jones S. M., Olivier S. S., Zhao M., Bower B. A., Izatt J. A., Choi S., Laut S., Werner J. S., "Adaptive-optics optical coherence tomography for high-resolution and high-speed 3D retinal in vivo

imaging," Opt. Express 13(21), 8532–8546 (2005).10.1364/OPEX.13.008532

17. Hammer D. X., Ferguson R. D., Bigelow C. E., Iftimia N. V., Ustun T. E., Burns S. A., "Adaptive optics scanning laser ophthalmoscope for stabilized retinal imaging," Opt. Express 14(8), 3354–3367 (2006).10.1364/OE.14.003354

18. Burns S. A., Tumbar R., Elsner A. E., Ferguson D., Hammer D. X., "Large-field-of-view, modular, stabilized, adaptive-optics-based scanning laser ophthalmoscope," J. Opt. Soc. Am. A 24(5), 1313–1326 (2007).10.1364/JOSAA.24.001313

19. Rha J., Schroeder B., Godara P., Carroll J., "Variable optical activation of human cone photoreceptors visualized using a short coherence light source," Opt. Lett. 34(24), 3782–3784 (2009).10.1364/OL.34.003782

20. Dubra A., Sulai Y., "Reflective afocal broadband adaptive optics scanning ophthalmoscope," Biomed. Opt. Express 2(6), 1757–1768 (2011).10.1364/BOE.2.001757

21. Ivers K. M., Li C., Patel N., Sredar N., Luo X., Queener H., Harwerth R. S., Porter J., "Reproducibility of measuring lamina cribrosa pore geometry in human and nonhuman primates with in vivo adaptive optics imaging," Invest. Ophthalmol. Vis. Sci. 52(8), 5473–5480 (2011).10.1167/iovs.11-7347

22. Dees E. W., Dubra A., Baraas R. C., "Variability in parafoveal cone mosaic in normal trichromatic individuals," Biomed. Opt. Express 2(5), 1351–1358 (2011).10.1364/BOE.2.001351

23. Hunter J. J., Masella B., Dubra A., Sharma R., Yin L., Merigan W. H., Palczewska G., Palczewski K., Williams D. R., "Images of photoreceptors in living primate eyes using adaptive optics two-photon ophthalmoscopy," Biomed. Opt. Express 2(1), 139–148 (2011).10.1364/BOE.2.000139

24. Vohnsen B., Rativa D., "Ultrasmall spot size scanning laser ophthalmoscopy," Biomed. Opt. Express 2(6), 1597–1609 (2011).10.1364/BOE.2.001597

25. Tojo N., Nakamura T., Fuchizawa C., Oiwake T., Hayashi A., "Adaptive optics fundus images of cone photoreceptors in the macula of patients with retinitis pigmentosa," Clin. Ophthalmol. 7, 203–210 (2013).

26. Zhang Y., Rha J., Jonnal R. S., Miller D. T., "Indiana university AO-OCT system," in Adaptive optics for vision science: Principles, practices, design and applications, Porter J., Queener H. M., Lin J. E., Thorn K., Awwal A., editors. , eds. (John Wiley & Sons, Inc., Hoboken, NJ, 2006), pp. 447–486.

27. Biss D. P., Webb R. H., Zhou Y., Bifano T. G., Zamiri P., Lin C. P., "An adaptive optics biomicroscope for mouse retinal imaging," (Proc of SPIE, San Jose, CA, 2007).10.1117/12.707531

28. Hofer H., Sredar N., Queener H., Li C., Porter J., "Wavefront sensorless adaptive optics ophthalmoscopy in the human eye," Opt. Express 19(15), 14160–14171 (2011).10.1364/OE.19.014160

29. Jian Y., Xu J., Gradowski M. A., Bonora S., Zawadzki R. J., Sarunic M. V., "Wavefront sensorless adaptive optics optical coherence tomography for in vivo retinal imaging in mice," Biomed. Opt. Express 5(2), 547–559 (2014).10.1364/BOE.5.000547

30. Sauvage J. F., Fusco T., Rousset G., Petit C., "Calibration and precompensation of noncommon path aberrations for extreme adaptive optics," J. Opt. Soc. Am. A 24(8), 2334–2346 (2007).10.1364/JOSAA.24.002334

31. Bloemhof E. E., Dekany R. G., "Metrology for the adaptive optics system at the Palomar 200-in. telescope," Proc. SPIE 3353, 638–648 (1998).

32. Porter J., Queener H., Lin J., Thorn K., Awwal A., eds., Adaptive Optics for Vision Science: Principles, Practices, Design, and Applications, Microwave and Optical Engineering (John Wiley & Sons, Inc, Hoboken, NJ, 2006).

33. Torti C., Povazay B., Hofer B., Unterhuber A., Carroll J., Ahnelt P. K., Drexler W., "Adaptive optics optical coherence tomography at 120,000 depth scans/s for non-invasive cellular phenotyping of the living human retina," Opt. Express 17(22), 19382–19400 (2009).10.1364/OE.17.019382

34. Zawadzki R. J., Jones S. M., Pilli S., Balderas-Mata S., Kim D. Y., Olivier S. S., Werner J. S., "Integrated adaptive optics optical coherence tomography and adaptive optics scanning laser ophthalmoscope system for simultaneous cellular resolution in vivo retinal imaging," Biomed. Opt. Express 2(6), 1674–1686 (2011).10.1364/BOE.2.001674

35. Ferguson R. D., Mujat M., Patel A. H., Iftimia N. V., "Making Ophthalmic Adaptive Optics Imaging More Adaptive," in Imaging and Applied Optics, OSA Technical Digest (online) (2013), OM4A.1.

36. Debarre D., Booth M. J., Wilson T., "Image based adaptive optics through optimisation of low spatial frequencies," Opt. Express 15(13), 8176–8190 (2007).10.1364/OE.15.008176

37. Débarre D., Botcherby E. J., Watanabe T., Srinivas S., Booth M. J., Wilson T., "Image-based adaptive optics for two-photon microscopy," Opt. Lett. 34(16), 2495–2497 (2009).10.1364/OL.34.002495

38. Wilson T., Carlini A. R., "Size of the detector in confocal imaging systems," Opt. Lett. 12(4), 227–229 (1987).10.1364/OL.12.000227

39. Booth M. J., Neil M. A., Juskaitis R., Wilson T., "Adaptive aberration correction in a confocal microscope," Proc. Natl. Acad. Sci. U.S.A. 99(9), 5788–5792 (2002).10.1073/pnas.082544799

40. Wright A. J., Poland S. P., Girkin J. M., Freudiger C. W., Evans C. L., Xie X. S., "Adaptive optics for enhanced signal in CARS microscopy," Opt. Express 15(26), 18209–18219 (2007).10.1364/OE.15.018209

41. Muller R. A., Buffington A., "Real-time correction of atmospherically degraded telescope images through image sharpening," J. Opt. Soc. Am. 64(9), 1200–1210 (1974).10.1364/JOSA.64.001200

42. Erteza A., "Sharpness index and its application to focus control," Appl. Opt. 15(4), 877–881 (1976).10.1364/AO.15.000877

43. Erteza A., "Depth of convergence of a sharpness index autofocus system," Appl. Opt. 16(8), 2273–2278 (1977).10.1364/AO.16.002273

44. Groen F. C. A., Young I. T., Ligthart G., "A comparison of different focus functions for use in autofocus algorithms," Cytometry 6(2), 81–91 (1985).10.1002/cyto.990060202

45. Firestone L., Cook K., Culp K., Talsania N., Preston K., Jr., "Comparison of autofocus methods for automated microscopy," Cytometry 12(3), 195–206 (1991).10.1002/cyto.990120302

46. Fienup J. R., Miller J. J., "Aberration correction by maximizing generalized sharpness metrics," J. Opt. Soc. Am. A 20(4), 609–620 (2003).10.1364/JOSAA.20.000609

47. Wang B., Booth M. J., "Optimum deformable mirror modes for sensorless adaptive optics," Opt. Commun. 282(23), 4467–4474 (2009).10.1016/j.optcom.2009.08.010

48. Albert O., Sherman L., Mourou G., Norris T. B., Vdovin G., "Smart microscope: an adaptive optics learning system for aberration correction in multiphoton confocal microscopy," Opt. Lett. 25(1), 52–54 (2000).10.1364/OL.25.000052

49. A. Dubra and Z. Harvey, "Registration of 2D Images from Fast Scanning Ophthalmic Instruments," in *The 4th International Workshop on Biomedical Image Registration*, (2010)10.1007/978-3-642-14366-3_6

50. Jonnal R. S., Besecker J. R., Derby J. C., Kocaoglu O. P., Cense B., Gao W., Wang Q., Miller D. T., "Imaging outer segment renewal in living human cone photoreceptors," Opt. Express 18(5), 5257–5270 (2010).10.1364/OE.18.005257

51. Cooper R. F., Dubis A. M., Pavaskar A., Rha J., Dubra A., Carroll J., "Spatial and temporal variation of rod photoreceptor reflectance in the human retina," Biomed. Opt. Express 2(9), 2577–2589 (2011).10.1364/BOE.2.002577

52. Hofer H., Chen L., Yoon G. Y., Singer B., Yamauchi Y., Williams D. R., "Improvement in retinal image quality with dynamic correction of the eye's aberrations," Opt. Express 8(11), 631–643 (2001).10.1364/OE.8.000631

53. Sulai Y. N., Dubra A., "Adaptive optics scanning ophthalmoscopy with annular pupils," Biomed. Opt. Express 3(7), 1647–1661 (2012).10.1364/BOE.3.001647